Composites Science and Technology 271 (2025) 111354

Contents lists available at ScienceDirect

Composites Science and Technology

journal homepage: www.elsevier.com/locate/compscitech

Decoupling the effects of topographical roughness and oxidation on the interfacial properties of carbon fiber-epoxy composites

Filip Vuković [a,b,*], Ben Newman [a], Yanting Yin [c,d], Gunther G. Andersson [c,d], Luke C. Henderson [e], Tiffany R. Walsh [a,**]

[a] Institute for Frontier Materials, Deakin University, Geelong, VIC 3216, Australia
[b] Institute of Applied Physics, TU Wien, Vienna 1040, Austria
[c] Flinders Institute for Nanoscale Science and Technology, Flinders University, Adelaide, SA 5042, Australia
[d] Flinders Microscopy and Microanalysis, College of Science and Engineering, Flinders University, Adelaide, SA 5042, Australia
[e] Carbon Nexus, Institute for Frontier Materials, Deakin University, Geelong, VIC 3216, Australia

ARTICLE INFO

Keywords:
Carbon fiber polymer composites
Interfaces
Oxidation
Molecular dynamics simulation
Epoxy

ABSTRACT

Carbon fiber composites under mechanical loading conditions must effectively transfer stresses from the relatively weak structural polymer matrix to the load-bearing carbon fiber. Oxidation treatments of the carbon fiber surface are a common strategy for improving the interface between fiber and matrix, and is understood to increase both the fiber surface roughness, as well as modify the fiber surface chemistry for better resin compatibility. However, it is challenging to decouple the effects of oxidation treatments on the fiber–matrix interface by experiment alone. Here, molecular dynamics simulations of topographically rough carbon fiber surfaces, both with and without oxidation, are interfaced with a thermoset epoxy matrix to decouple the impact of surface roughness and chemical interactions on the interfacial interaction between fiber and matrix. Smoother surfaces yield a greater enhancement of interfacial shear stress in fiber displacement simulations after oxidation, with the pristine graphite surface yielding the greatest increase relative to its non-oxidized value. Additionally, the results suggest that nanoscale fiber surface corrugation perpendicular to the fiber axis could be employed as a strategy to enhance the interfacial shear strength of composites. Overall, these simulations provide nanoscale insights regarding the interplay between surface roughness and chemistry of composite interfaces, which may inform future fiber surface treatments.

1. Introduction

Carbon fiber reinforced composite (CFRC) materials are prevalent in high-performance structural applications where weight is a critical factor, due to their excellent mechanical properties and low specific weight relative to traditional engineering metals. A more recent and increasingly important application of CFRCs is the reduction of mass in structural components as a strategy for reducing emissions, which has been employed in both the aviation [1,2] and transport sectors [3,4]. Being a composite material, the juncture between carbon fiber (CF) and polymer matrix, herein referred to as the CF-matrix interface, plays a vital role in the stress transfer from the load bearing CFs to the relatively weak polymer matrix, and may ultimately limit the mechanical performances of the composite as debonding is a common failure mode [5,6]. In an effort to improve the interface quality between fiber and matrix, the CF surface and the modification thereof has been the focus of many recent studies of the CFRC interface [7–9]. It is thought that these treatments work by (i) by increasing fiber surface roughness by either etching the carbon surface itself or creating a textured surface with the addition of new chemical groups, and/or (ii) by introducing additional chemical interactions between the fiber surface and the matrix. However, it remains challenging to decouple these effects not only due to the limited spatial and temporal resolution of traditional experimental methods, but also the lack of realistic atomistic models of the CF surface that incorporate roughness.

Surface oxidation treatments of the CF have been known to improve the CFRC interfacial bond since the commercialization of CF, and remains an important step in modern CF production. It is understood that oxidation treatments not only increase the amount of oxygen bearing functional groups covalently bound to the CF, but also etch and roughen the CF surface [10–13]. These factors, coupled with the additional complication of the matrix response which may also vary depending on chemical composition, topology and spatial structure of

* Corresponding author at: Institute of Applied Physics, TU Wien, Vienna 1040, Austria.
** Corresponding author.
E-mail addresses: vukovic@iap.tuwien.ac.at (F. Vuković), tiffany.walsh@deakin.edu.au (T.R. Walsh).

https://doi.org/10.1016/j.compscitech.2025.111354
Received 5 May 2025; Received in revised form 5 August 2025; Accepted 21 August 2025
Available online 28 August 2025

the network, as well as the overall degree of crosslinking (DoC) of the resin, all affect the quality of the interfacial bond between fiber and matrix. Here, molecular dynamics (MD) simulations can provide insights regarding the molecular interactions at the CF-matrix interface, not only because of the short lengthscale and fine timescale resolution compared to many experimental techniques, but also because of the ability to purposely craft idealized, de-coupled, and comparative simulations that can isolate these factors to explore the mechanistic origins of interfacial stress transfer. In particular, MD simulations have played a key role in identifying and designing chemical functionalization of the CF surface as a viable strategy in enhancing the interfacial shear strength of the composite [7,14–16]. Here, simulations were used to study the possible molecular mechanisms of these covalent functionalizations and their effects on the interfacial shear stress (ISS), which is a commonly used proxy for the interfacial shear *strength*, IFSS (not to be confused with the interfacial shear stress [17]), and has informed the design of bespoke functional groups specifically designed to improve the ISS of CFRCs [18].

In the simulation literature of carbon fiber-polymer interfaces, graphite is typically used as a surrogate model for the carbon fiber surface. Within this approximation, many reports have investigated surface roughening and its impact on the mechanical properties of several related carbon-polymer interfaces, e.g. graphite defects, graphite orientation, surface wrinkling related carbon-polymer interfaces [19–29]. While graphite remains an adequate surrogate for the CF surface for many CFRC interface simulations, capturing the mechanical response of a *pristine* CF-matrix interface under CF displacement loading remains challenging. A recent report by Sohail et al. used an experimentally guided approach, where Fourier-series decomposition of atomic force microscopy (AFM) images of the CF surface profile were used to inform MD simulations from which a length-scale averaged shear stress could be back-calculated [24]. While the shear stresses predicted by this method are comparable to experimental data, it is not able to elucidate the interplay between nanoscale roughness and oxidation chemistry on the mechanical performance. Recent simulations reported by Li et al. represent a major step forward in CF surface modeling [30]. The authors produced turbostratic CF surfaces by heating and compressing graphite flakes into trapizoidal surface shapes, and interfaced these models with a two-part epoxy for further simulation. These authors report that higher protrusion of the CF surface into the matrix enhances tensile strength for both perpendicular and shear stress loadings.

Disparate from surface roughness effects, the link between oxygen content on the CF surface and improved ISS has been experimentally established for some time [11,12,31–35]. There have been numerous simulation studies that have sought to elucidate the effect of oxygen bearing functional groups on the composite interface. Semoto et al. [36] reported density functional theory (DFT) simulations of a bisphenol-A diglycidyl ether (DEGEBA) fragment *in-vacuo* pulled along a graphite edge functionalized with hydroxyl and carboxbylic acid groups. Graphite edges functionalized with carboxylic acid groups were found to have a greater interaction energy with the epoxy polymer fragment relative to the hydroxyl, and both graphite edge models were observed to interact via hydrogen bonding with the polymer fragment. Further DFT simulations have explored interactions of a DAGEBA and diaminodiphenyl solfone oligomer unit absorbed onto graphene and oxidized (hydroxyl and epoxy) graphene surfaces [37]. The authors report that dispersion interactions were similar for both graphene and oxidized graphene, whereas oxidized graphene was found to foster significant hydrogen bonding between the hydroxyl, epoxy, amine and sulfonyl groups present in the oligomer and at the oxidized graphene surface. Early MD simulations of oxidized composite interfaces were reported by Jang et al. [38], where shingle stacked graphite flakes functionalized with hydroxyl, epoxy and carbonyl groups, were interfaced with a vinyl ester *liquid* (not-cured resin) to study the near-interface liquid structuring. Recent experimental and MD simulations of both pristine and hydroxylated graphite interfaced with an epoxy resin agglomeration consisting of DGEBA and methyl hexahydrophthalic anhydride (MeHHPA), were reported by Wang et al. [39]. The authors reported that the interfacial energy change under substrate displacement simulations was greater for the oxidized composites. However, this work used a pre-packed matrix preparation approach, and therefore could not capture the interphase of the composite interface. Furthermore, the modeling of functional COOH groups did not take into account the chemistry of how these groups would form under oxidation conditions, i.e. they were simply attached to the basal graphite plane.

Related to oxidized CF-polymer interfaces, Li et al. [40] reported coarse-grain MD simulations of graphene oxide interfaced with a polybutadiene polymer matrix explored the impact of oxygen group heterogeneity in graphene-oxide polymer composites. The authors reported that non-uniform distributions of oxidized domains of the graphene would template heterogeneity into the polymer matrix density in the interphase, indicating that the distribution of oxygen functional groups may impact the structure of the epoxy matrix in the CFRC interphase. Small oxygen bearing functional groups covalently attached to the graphite surface have been extensively reported in the literature, however there is a general lack of integration of chemical intuition regarding how and where these groups would form on the CF surface, mainly due to the limitations of using graphite as a surrogate structural model for CF.

Here, MD simulations of both oxidized and non-oxidized CF surfaces were performed to explore the impact of nanoscale surface roughness, thought to be inherent to the CF surface, and oxygen chemistry on the mechanical properties of the CFRC interface. Structural models of the CF surface reported by Vuković and Walsh [41] go beyond the typical planar graphite surrogate, employing reactive MD simulations to generate topographically rich CF surfaces which can then be translated to a more suitable fixed-topology force field capable of modeling polymer-fiber interfaces. Three distinct types of surface roughness were investigated: globally flat surfaces that feature short-range roughness with amplitudes on the order of a few Ångstroms, similar in quality to commercial abrasive paper; relatively smooth surfaces that feature long-range global corrugation and exposed graphitic carbon edges; and the idealized perfectly flat graphite surface. Herein the first surface model will be referred to as sandpaper CF, and the second will be referred to as hills CF. The rough CF surfaces were interfaced with a typical structural epoxy of bisphenol F diglycidyl ether (commercially referred to as EPON-862, and herein referred to as EPON for short) and diethyl toluenediamine (DETDA). The effects of *significant* levels of surface oxidation were also explored for all CF surfaces. The CF surface models used herein represent a significant step beyond the typical models of the CF surface employed to-date.

2. Methods

2.1. General simulation details

CF structural models were generated using a multi-stage process which is discussed in the following section, however all production simulations of the composite interfaces were performed using the LAMMPS software package [42], employing GPU acceleration where possible [43–48]. These composite simulations employed the DREIDING force field [49], using the Buckingham function for pair-wise interactions ($\zeta = 12$) with no additional hydrogen bonding terms. Van-der Waals interactions were truncated and shifted at 12 Å, and electrostatics beyond the same cutoff distance were calculated using the particle–particle–particle mesh method [44]. The DREIDING force field has been used successfully in previous carbon-polymer interface MD simulations [17,50] and is therefore used here to ensure comparability with these prior simulation efforts. The equations of motion were integrated using a timestep of 1 fs, and temperature and pressures were controlled using the Nosé-Hoover thermostat and barostat, for the *NVT* and *NPT* ensembles, respectively, unless otherwise specified. All analyses were performed using in-house codes.

2.2. Carbon fiber surface models

Two distinct topographically complex CF models were generated as per the methodology established in Ref. [41]. In brief, each CF surface model was generated using reactive MD simulations with the carbon-only EDIP potential [51]. A slab-like geometry is achieved by introducing a vacuum gap during the annealing stage, forming a carbon slab with an upper and lower surface. Two types of surface roughness were generated by varying the annealing temperature and time, resulting in one CF slab with short-ranged roughness termed 'sandpaper', and another with smoother exposed surfaces with longer length-scale undulations termed 'hills'. The sandpaper CF was generated using an annealing temperature of 3000 K and was annealed for 50 ps, whereas the hills CF was annealed at 3000 K for 400 ps. These carbon-only structures were then passivated by either saturating graphitic edges and under-coordinated carbons with hydrogen, or oxidized as per the methodology described in the following section. The passivated structures were then ported to a fixed-topology description suitable for use with the DREIDING potential. Partial charges were assigned to unique atom types based on charge values as calculated using the charge equilibration (qEq) method [52], as per the DREIDING specification. For each element present, similar chemical environments were classified and given a unique atom type, and partial charge values were averaged over all atoms within a given type. This process results in a small amount of residual total charge for the unit cell, which was then redistributed over the atom types to ensure net-zero charge of the entire CF substrate. Unit cell dimensions in x and y were approximately 100 Å long, with an approximate slab thickness of around 15 Å, and were thus comparable in dimension to the idealized graphite substrates used in previous works [15,50]. All the carbon and hydrogen only CF models are herein referred to as 'plain' to distinguish them from their oxidized counterparts.

2.2.1. Oxidation of CF surfaces

A total of three oxidized CF models were used for the oxidized composite simulations: oxidized versions of each of the two rough CF surface models (sandpaper and hills), as well as an oxidized four-layer graphite substrate. An overall 0.3 O/C ratio was targeted, as informed by X-ray photoelectron spectroscopy (XPS) of pristine, and electrochemically oxidized CFs under various currents and exposure times (Section S2.1 in the SI). All CF models were oxidized using an in-house code named 'CarbOx', which can install simple oxygen bearing chemical groups on general atomistic carbon structures given a standard coordinate input file. This code has been made freely available for use under the GPL-3.0 license [53].

The three CF surfaces were oxidized according to the following algorithm. Two general types of carbon were identified for oxidation within the CF models: edge carbon which refers to under-coordinated atoms, and so-called 'surface' carbon. Here, surface carbon refers to atoms that constitute the upper and lower surfaces of the slab-geometry CF models. A surface mesh generation algorithm was used to identify surface atoms [54–56]. Surface meshes were generated using a probe radius of 3.5 Å, and atoms that form these defined surfaces were deemed to be 'surface', with all other atoms then designated as 'interior' sites. It should be noted that due to the disordered and porous nature of the CF models, particularly the hills CF, carbon atoms that bordered the few porous domains present within the CF interior were identified as surface carbons. This was not deemed to be an issue, and as such these sites were similarly considered as eligible surface carbons.

Oxygen bearing functional groups were selected based on experimental reports of oxidation treatments of CF and related carbon materials (e.g. XPS, Fourier-transform infrared spectroscopy, and ^{13}C nuclear magnetic resonance spectroscopy) [12,57–59]. The results of previous MD simulation studies of graphene oxide reduction were also considered [60]. First, all edge and under-coordinated carbon sites were selected for oxidation, and three potential functional groups could be covalently attached at these sites: carboxylic acid, carbonyl, or hydrogen. A preference of carboxylic acid over carbonyl was given with a probability of 0.6 to 0.4, as determined from a previous simulation study of graphene oxide reduction [60]. If the oxidation algorithm was unable to physically accommodate the specified group onto a particular edge site due to steric hindrance, then the site was instead passivated with a single hydrogen.

With all under-coordinated carbons saturated, surface sp^2 carbon sites were then oxidized such that the total O/C ratios were comparable to the experimental XPS values. A possibility of two functional groups could be installed at designated surface (sp^2) carbon site: hydroxyl, and epoxy. Hydroxyl functionalization was given a probability preference over epoxy of 0.7 to 0.3 [60]. As was the case for edge carbon functionalization, if the group could not be fit at the target carbon site due to overlap with surrounding atoms, then it was rejected and not installed. This resulted in oxygen groups being installed on roughly 70 % of the surface carbon sites in the hills CF and slightly less for the sandpaper CF given the larger proportion of edge carbon present in the latter. Details regarding the final compositions of the oxidized CF models are provided in Table 1 in Section 3.1 of the Results.

Additionally, oxygen groups attached at surface carbon sites were installed with the appropriate orientation, directed away from the CF bulk and up towards the vacuum gap. This posed an additional challenge as corrugations were present in the rough CF models, particularly in the hills CF, meaning that carbons could not be defined as belonging to either the upper or lower surface just by the absolute z coordinate of the carbon alone. To determine which surface a particular surface carbon belonged to, a local cylindrical domain of CF carbons were selected within a radius 5 Å away from the target surface carbon was used to determine the thickness and height profile of the CF local to the target site. If the target surface carbon was in the upper half of this local CF domain, then the functional group was installed projecting towards the upper cell boundary, otherwise the functional group was flipped to project towards the lower cell boundary. This procedure ensured that functional groups were installed on the outer surfaces of the CF, as would most likely be the case in the real scenario. Due to the complexities in defining a CF surface as well as the presence of both interior under-coordinated carbons and interior graphitic edges, this procedure resulted in a small amount of sub-surface oxidation.

The third oxidized CF model consisted four-layers of graphite lattice stacked in an ABAB pattern, with similar simulation cell dimensions to the two rough CF models. As there were no edge or under-coordinated carbons in the graphite slab, only hydroxyl and epoxy groups were installed onto the two outer surfaces of the graphite slab and no sub-surface oxidation was permitted.

Partial charges were assigned to the functional groups and their neighboring carbons, with partial charge values balanced within the functional group such that each group was charge neutral. Calculation of these partial charge values was performed using a vacuum gap between the upper and lower CF surfaces of $\sim$ 60 Å using periodic boundary conditions for x and y unit cell boundaries, and a non-periodic condition in the z boundary, making the appropriate slab geometry corrections for the long-range electrostatic contributions. The calculation was performed for both the oxidized sandpaper and oxidized hills models, and resulted in similar charge values for like oxygen groups. These values were then slightly adjusted so that general partial charge values could be used for atoms within each oxygen group, thereby maintaining charge neutrality within the simulation cell. A table of partial charge values used in these simulations is provided in the SI (Tables S1 and S2).

2.3. Modeling the composite interfaces

The plain and oxidized CF slabs, as well as the oxidized graphite, were then interfaced with a liquid epoxy precursor mixture, which was subsequently crosslinked to form an epoxy network. First, a vacuum

gap was introduced to the unit cell above the CF slab, and a precursor mixture 1600 EPON and 800 DETDA monomers was subsequently packed into the gap at low density using a combination of the PACKMOL [61] and MOLTEMPLATE [62] software packages. This resulted in a liquid mixture with a stoichiometric ratio of 2:1, which theoretically permits every epoxy group in the resin to form a crosslink bond during cure. Two simulation replicas of each precursor system were made, which were independently brought to equilibrium density by sampling different initial velocity distributions, resulting in a total of six independent CF precursor composites. The CF-liquid precursors were brought to an equilibrium density at 500 K (the approximate experimental curing temperature for an EPON-DETDA epoxy resin) over 2 ns of anisotropic *NPT* simulation at 1 atm of pressure. Density profiles shown in Figure S6 of the SI indicate that equilibrium density was achieved within the first 300 ps of dynamics. The precursor composites were then subjected to a series of simulated annealing cycles to ensure that the liquid was thoroughly mixed and equilibrated in the presence of the CF surfaces. Further details regarding the simulated annealing are provided in the SI. Separate linear mass density profiles of EPON and DETDA were calculated perpendicular to the CF surface (along the **z** coordinate) after each successive simulated annealing cycle. The convergence of these mass density profiles was used to monitor the liquid mixture, from which five simulated annealing cycles were determined to be sufficient.

Being a fixed-topology force field, DREIDING has no in-built provisions to model covalent chemical reactions. Crosslinking of the epoxy was therefore achieved by employing the REACTER protocol of Gissinger et al. [63,64], which enables the breaking and forming of covalent bonds within traditional fixed-topology force fields. Each EPON monomer bears two reactive epoxy groups that are permitted to react with the two amine groups on the DETA monomers. Amine groups in their unreacted state, known as primary amine, are able to undergo two crosslink reactions, becoming a secondary and tertiary amine with each successive reaction. Unlike prior simulation studies of crosslinked epoxy networks and interfaces [50,65], here epoxy groups were initially modeled in their unreacted state, i.e. as a closed epoxy ring. During periods of simulation which are termed 'crosslinking dynamics', the formation of a crosslink bond was permitted to occur between any epoxy groups and amine groups (oxygen to nitrogen distance) separated by a distance less than the specified crosslinking cutoff distance r_c. In addition, for every timestep of crosslinking dynamics where an epoxy-amine pair satisfy the distance criteria, there is a 50 % probability of forming a crosslink bond. If a potential epoxy-amine pair is permitted to crosslink, the two sites undergo a crosslink procedure which is controlled by limited displacement dynamics within the REACTER scheme, separate from the global thermostat. First the epoxy ring is opened breaking the O-C bond, and a proton from the amine group is transferred from the nitrogen to the now-undercoordinated carbon. Subsequently, a bond is formed between the oxygen and nitrogen sites, completing the crosslink event. Bond topology and partial charges are updated during the event so that the total system remains charge neutral, and that electrostatics and non-bonded interactions are computed correctly following the event.

The final resin curing protocol used here was determined after significant testing with a pure EPON-DETDA polymer system. The results of these tests are discussed in Section S2.5 of the SI. A single round of crosslinking for a given cutoff distance consisted of (i) 500 ps of crosslinking dynamics at 500 K in the *NVT* ensemble, (ii) a further 200 ps of crosslinking dynamics in the *NPT* ensemble at 500 K and 1 atm, and (iii) a final stage of regular non-crosslinking *NVT* dynamics at 500 K. Two rounds of crosslinking were performed using a r_c = 3 Å and 4 Å. During crosslinking dynamics, van der Waals interactions were switched from the usual X6 functions to the Lennard-Jones description, to ensure stable dynamics during the crosslink events. This was done as the X6 functional form has catastrophic behavior at small separation distances, and while these separation distances are not typically seen accessible during regular dynamics, they can occur during crosslink events. Composites ultimately achieved a DoC of around 85 %, however, frames at 78 % DoC were used for further analysis to ensure that the results could be compared to prior graphite composites [50]. Graphs of the number of crosslink bonds as a function of simulation time for all samples are shown in the SI, Figures S10–S12.

With the resin matrix cured to 78 % DoC, van der Waals interactions were switched back to use the usual X6 description. The cured composite samples were subjected to 1 ns of *NPT* dynamics at 500 K and 1 atm using dual thermostats, one for the polymer network and another for the CF substrate. Samples were then cooled down to 300 K over 5 ps in the *NPT* ensemble, with a linear cooling rate of 4×10^{10} K s^{-1}, and maintaining 1 atm of pressure. With the composites at room temperature, each sample was then subjected to a further 2 ns of *NPT* dynamics at 300 K and 1 atm, or standard ambient temperature and pressure (SATP), prior to further analysis.

2.4. Analyses

The interfacial shear stress (ISS) of the composite interfaces was determined via CF substrate displacement simulations. To this end, the total potential energy difference was calculated for a CF displacement of 40 Å, to maintain comparability with previously-published simulations. The total potential energy was recorded every fs, and curves were smoothed using a uniform linear filter with a window of 1000 data points. Only the CF carbon atoms were frozen and displaced during the displacement simulations, i.e. polymer atoms and the functional groups attached to the CF were not frozen. All free atoms were thermostatted using the Langevin thermostat at 300 K and permitted to move according to the forces acting on them. The CF was displaced at a rate of 0.5 Å ps^{-1}. This strain rate is orders of magnitude larger than typical experimental rates, which is necessary given the limited timescales that are practically accessible to MD simulations. As such, we do not directly compare absolute predicted ISS values to their experimental counterparts, and instead focus on the relative differences between the different systems modeled. Two CF displacement simulations were performed for each composite replica sample, one displacing the CF along the x coordinate, and another displacing along y. It is worth noting that for the hills composites, CF displacement along x aligns parallel with the global corrugation axis, whereas CF displacement along y is perpendicular to the corrugation. To calculate the ISS, the work done displacing the CF may be related to the ISS, τ, via the equation [17]

$$\frac{W}{l} = 2\tau L_x L_y, \tag{1}$$

where L_x and L_y are the x and y dimensions of the CF slab, l is the displacement distance, and W is the change in total potential energy. A table of unit cell dimensions for all crosslinked and cooled composites is provided in the SI (Table S4).

To quantify the mechanical response of the polymer matrix under substrate displacement, displacement vectors of polymer atoms were calculated and decomposed into components lateral and transverse to CF displacement, and were then spatially binned along the z coordinate which is perpendicular to the CF surface. More specifically, the displacement vectors of atomic position for polymer atoms between 0 and 40 Å of CF displacement were decomposed into components that moved parallel with the CF displacement (longitudinal), and perpendicular to the CF (transverse) were spatially binned along the z coordinate perpendicular to the CF surface and normalized by the bin volume. A spatial grid of 100 bins was used for all composites, which results in a bin width of around 1 Å, due to the differences in unit cell dimensions between the different composites.

Sub-networks within the matrix were identified within the polymer using a graph theory approach, where each monomer is treated as a node and crosslink bonds between monomer units were taken to be edges. Mass density profiles were calculated for each of these sub-networks along the z axis perpendicular to the CF surface over 300 ps

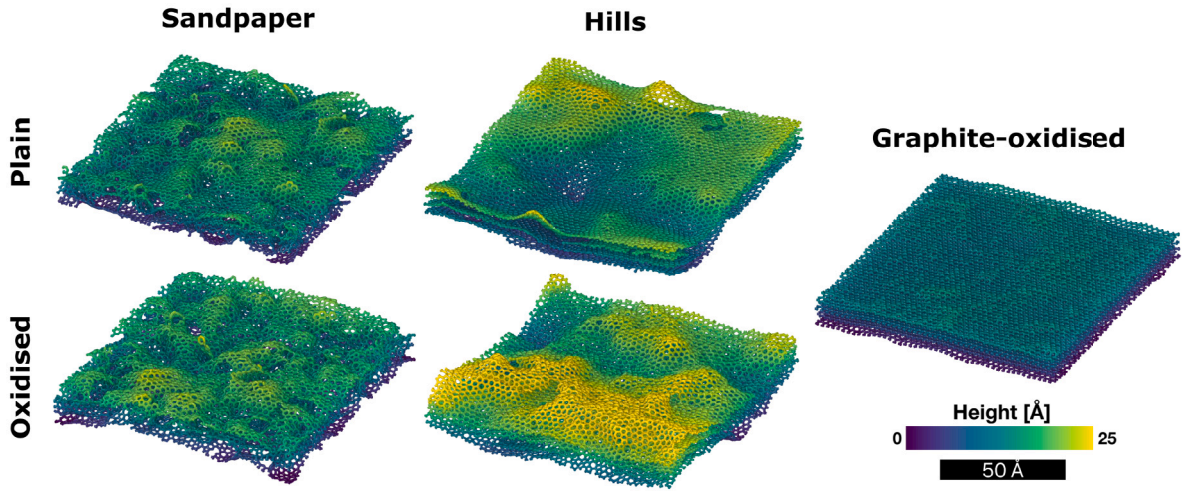

Fig. 1. Images of the CF substrates showing only carbon atoms, i.e. hydrogen and oxygen have been removed for visual clarity, and colored according to height profile. These images illustrate the difference in both range and scale of roughness between the sandpaper and hills CFs. All substrates have been translated such that $z = 0$ is in plane with the lowest carbon atom.

of *NPT* simulation at 300 K and 1 atm, after cooling. Profiles sampled simulation frames every picosecond, resulting in a total of 301 frames used for the calculation. Once more, 100 spatial bins along the z unit cell direction were used for this calculation.

3. Results and discussion

3.1. CF substrate, liquid precursor, and composite characterization

A total of five unique CF composite interfaces were explored: two featuring CFs with no oxidation and distinct nanoscale roughness of the CF, two with CFs that feature both nanoscale roughness and heavy oxidation CF surfaces, and a final composite that features a topographically smooth and heavily oxidized graphite CF surrogate. Two replica simulations were performed for each of these unique composites. For the non-oxidized CF, which will be referred to as 'plain' CF composites, two distinct variations of nanoscale roughness were modeled. The first featured disordered carbon topology with high frequency roughness with surface fluctuations on the order of several angstroms and was globally flat, referred to as the sandpaper CF. The second plain CF featured smoother graphitic topology, lower frequency roughness, and greater surface height fluctuations, as well as global corrugations that were aligned along the x unit cell axis, referred to as hills CF. For the oxidized CF composites, both sandpaper and hills CF models were heavily oxidized via the introduction of covalently bonded oxygen bearing functional groups. The third oxidized composite comprised a four-layer graphite model of CF with similar levels of surface oxidation.

Fig. 1 presents images of all CF models showing only the carbon atoms which have been color coded according to height, where the CF has been translated such that the lowest carbon atom is at $z = 0$. While it is challenging to quantify the difference in roughness character between the plain sandpaper and plain hills surfaces, these images illustrate a clear qualitative difference between the two. It can also be seen that the oxidation of the CF models has induced further roughness into the CF surfaces, and is particularly apparent for the hills CF. Two mechanisms are likely inducing the additional roughness in the oxidized CF surfaces, (i) surface sp^2 carbon adopting sp^3 geometry after functionalization, and (ii) strong hydrogen bonding interactions between sub-surface oxygen groups located at internal graphitic edges which can strain the CF surface. Fig. 2 presents a schematic of the proposed oxidized edge hydrogen bonding induced additional roughness, illustrating how the attractive interactions between oxidized interior sheet edges may induce additional surface topography. The inset image presents an example of this interior edge oxygen group interaction occurring between several carboxylic acid and carbonyl groups on two graphitic sheet edges in the hills-oxidized CF model.

In the case of the oxidized CF models, four functional groups were present: carboxylic acid and carbonyl, which were attached to edge and under-coordinated carbon sites, and hydroxyl and epoxy groups that were attached to sp^2 surface carbons only. Table 2 presents the atomic decomposition of each of these CF models. Much of the smooth character of the hills CF surface may be attributed to the higher fraction of sp^2 carbons which forms graphitic surfaces and is approximately 10 % greater than that seen in the sandpaper CF.

Table 2
Absolute number of atoms and percentage breakdown of atomic composition for each CF substrate. The percentage of sp^2 C specifically refers to the percentage ratio of three-fold coordinated carbon to all other carbons.

System	Total atoms	O	H	C	sp^2 C
Sandpaper	19 212	0	6	94	87
Hills	18 312	0	3	97	99
Sandpaper-oxide	25 596	17	11	72	61
Hills-oxide	24 346	16	10	74	71
Graphite-oxide	23 843	10	7	83	85

Data from XPS experiments of both pristine CF and CF exposed to electrochemical oxidation for various lengths of time were used to determine maximal oxygen loading conditions for the CF models. Details of the XPS results and methodology are provided in the SI, Section S2.1. The results indicated that an O/C ratio of ~ 0.3 was the maximal amount of oxygen loading before the oxygen fraction drops with extended oxidation. Hence the oxidation of the CF models targeted a similar oxygen content fraction of around 0.3. Table 1 presents a

Table 1
Breakdown of functional groups in oxidized CF models.

System	O/C	COOH	CO	COOH/CO	Edge H	hydroxyl	Epoxy	Hydroxyl/epoxy
Graphite-oxide	0.12	0	0	0	0	1633	705	2.3
Sandpaper-oxide	0.24	458	398	1.2	34	2163	915	2.4
Hills-oxide	0.22	136	176	0.8	107	2301	1112	2.1

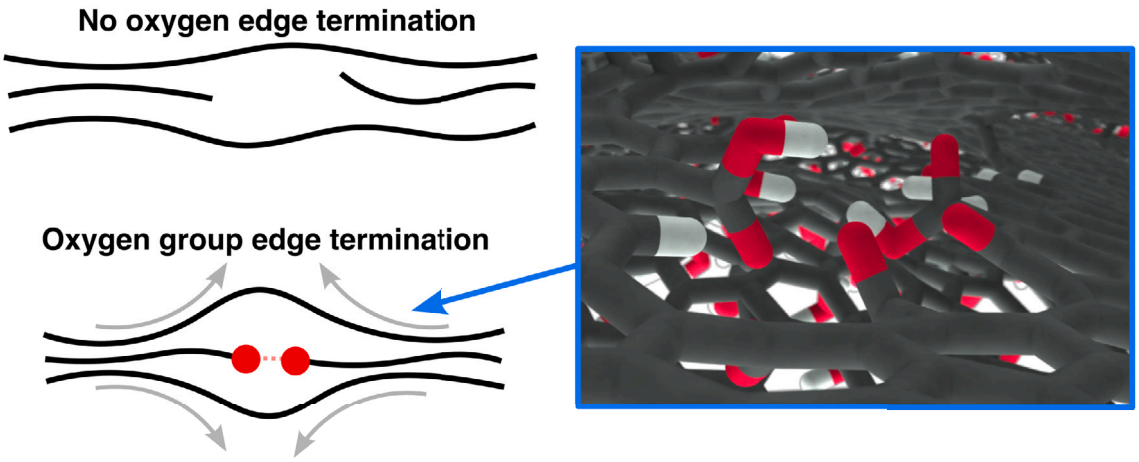

Fig. 2. Schematic of how interior edge oxidation may induce additional surface topography. Inset image in the blue box shows an example of this sub-surface hydrogen bonding interaction between functional groups on two nearby sub-surface graphitic edges in the oxidized hills CF. Carbon atoms are colored gray, oxygen in red, and hydrogen in white.

breakdown of the oxygen functional groups present in the oxidized CF models. The total O/C ratios of both the sandpaper-oxidized and hills-oxidized CFs was 0.24 and 0.22 respectively. Given that the CF models contain not only surface carbon available for functionalization, but also feature a small amount of interior sites, the actual surface O/C would be greater than that of the entire CF model, and was approximated to be slightly above 0.3 by considering only the first surface layer of carbon and oxygen. The graphite-oxide model has a considerably lower O/C ratio of 0.12 which is primarily due three factors: first, the flat pristine graphite lattice presents less surface area for functional groups to be installed; second, no carboxylic acid or carbonyl groups were present as there are no edge carbon; and third, as there were no holes or defects in the graphite there was no reason to install oxygen functional groups in the sub-surface layers. Considering only the top layer of the oxidized graphite model, the O/C ratio is ~ 0.24, close to the experimental XPS value of just under 0.3.

The plain CF models contain many topologically and topographically interesting surface structures, from standard graphite defects such as edges, vacancies, and non-hexagonal rings that induce surface curvature [66], to more complex and larger scale features such as sheet intersections, internal pores, and cave-entrance like structures. These topographical features provide the liquid polymer precursor mixture with a complex surface to interface with. Relative to both previously reported simulations of pristine graphite epoxy interfaces [50], as well as the relatively flat oxidized graphite liquid mixture composite, both the sandpaper and hills CFs do not permit structuring of the liquid epoxy to the same extent as these aforementioned flat CF surfaces. Mass density distributions (provided in the SI, Figures S7–S9) of the sandpaper CF show a weak density peak for both EPON and DETDA at the CF onset, and the sandpaper-oxidized CF presents a single weak peak at the CF onset for just EPON. The sandpaper CF surface structure also contained larger voids relative to the other CFs, which were directly exposed to the liquid precursor. Fig. 3 presents an image of the first monolayer of liquid epoxy mixture (with the CF and remainder of the liquid removed for clarity), where a monomer was defined to be part of the first monolayer if any of its constituent atoms was within 3 Å of the CF surface. An inset image shows this singular EPON monomer with the context of the CF surface. Many monomer units extend into the CF surface undulations and pores, however one entire EPON monomer was observed to be reside within a surface pore in both replica simulations of the plain sandpaper interface, and in replica one of the oxidized sandpaper liquid precursor. None of these embedded monomers formed crosslinks in the fully cured composites.

Similar mass density distribution behavior was observed for the plain and oxidized hills CFs, however it should be noted that the global curvature makes interpretation of the overall mass density distributions challenging as weak structuring at the CF surface would be lost in the overall mass density due to the fluctuation of surface height, as

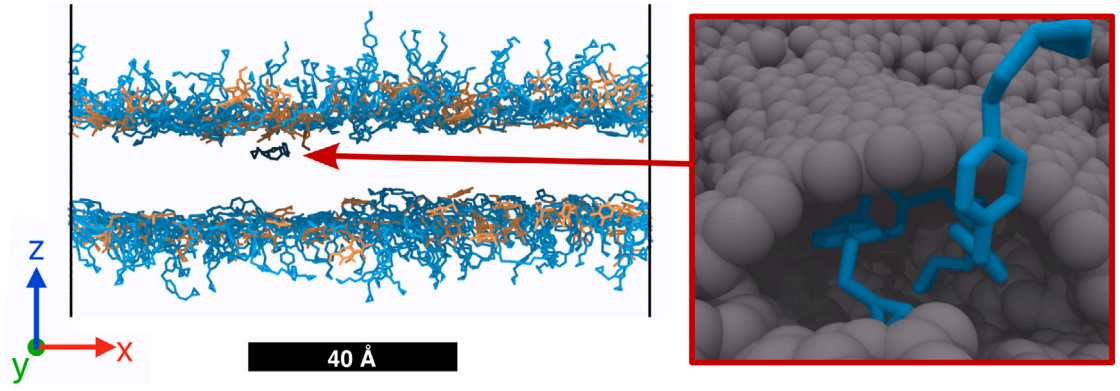

Fig. 3. Image of the first monolayer of liquid polymer at the CF surface (CF removed for visual clarity) of the plain sandpaper composite, where blue molecules are EPON, orange are DETDA, and the black lines denote the periodic boundary of the simulation cell. The red-bordered inset image shows a close-up of one sub-surface buried, and another partially buried EPON monomers, with all other monomers and non-carbon atoms removed for clarity.

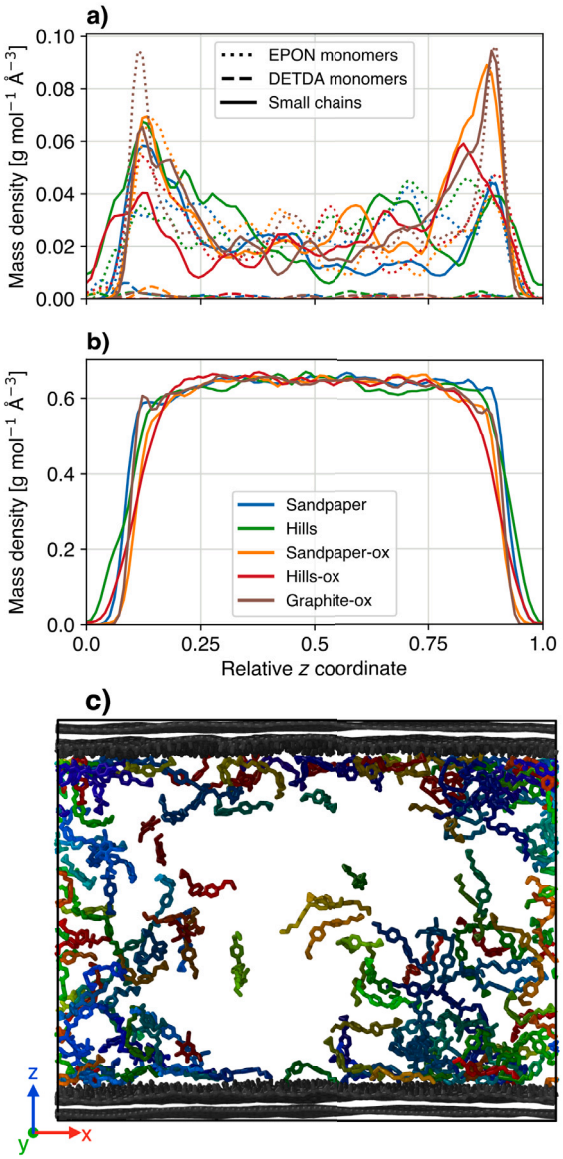

Fig. 4. Replica averaged mass density profiles of unreacted monomers and small disconnected network chains (a), and the dominant polymer network (b), binned along the z axis perpendicular to the CF surface. For reference, the CF approximately occupies the regions between relative $z = 0$ to 0.12, and $z = 0.88$ to 1. Visualization of the small polymer chains and unreacted monomers for the graphite-oxide composite (replica 1) is shown in panel (c), with the various disconnected chains shown in different colors. Here the dominant polymer network has been removed for visual clarity and atoms comprising the CF are colored gray.

mass density is averaged over slabs of volume perpendicular to the z direction. Comparatively strong liquid structuring was observed in the oxidized graphite composites, with at least two strong and distinct density peaks present at the CF onset for both EPON and DETDA. All liquid precursor composites were then crosslinked up to a DoC of 78 % and cooled to SATP conditions in the *NPT* ensemble for CF displacement simulations and further characterization.

The resultant crosslinked matrix topology was analyzed using a graph theory approach, revealing that all systems exhibited a similar polymer matrix structure: a dominant network that comprised majority of the monomer units, several small and disconnected networks, a few unreacted EPON monomers, and trace-to-no amounts of unreacted DETDA. Fig. 4 presents mass density distributions several components of the crosslinked polymer network, namely the loose unreacted monomers and small disconnected networks shown in panel (a), and the dominant network mass distribution shown in panel (b), plotted as a function of relative z coordinate. Here, a relative z coordinate is used so that composites with slightly different final unit cell dimensions may be more readily compared. An image of the disconnected networks and loose monomers for the oxidized graphite composite (replica 1) is shown in Panel (c) of Fig. 4. A concentration of both unreacted EPON monomer units, and small disconnected polymer networks at the polymer interphase is present and can be observed in Fig. 4a, noting that the CF-matrix interface is located at a relative z coordinate of approximately 0.12 and 0.88. This indicates that crucial polymer matrix interphase was inherently compromised in that there is a lower degree of main network connection in the interphase relative to the bulk polymer. It is worth noting that the very definition of an interphase requires a metric that is able to distinguish bulk-like behavior of a material from material that is affected by the presence of an interface. Here, it is suggested that not only should the polymer density be considered when classifying an interphase in polymer-x interfaces, but also the topological structure of the matrix should also be considered. Future research regarding the enhancement of mechanical interaction the CFRC interface should investigate this compromised polymer network topology at interfaces, in an effort to reduce this effect and increase the mechanical transfer of loads from CF to matrix.

3.2. CF displacement simulations and matrix response

The fully crosslinked composites were then subjected to CF displacement simulations to calculate the relative ISS and characterize the mechanical response and interactions of the CF matrix interface. Fig. 5 presents replica and displacement direction averaged potential energy difference curves as a function of CF displacement for all composites, where the shaded region of each curve represents one standard deviation from the mean value. In the case of the plain CF composite displacement simulations (blue and green curves), high frequency short lengthscale roughness was found to consistently result in a higher potential energy change up to ~ 25 Å of CF displacement. Beyond CF displacements of 25 Å, only when global corrugations of the smoother hills CF where perpendicular to the displacement direction could the potential energy difference curve match that of the sandpaper case.

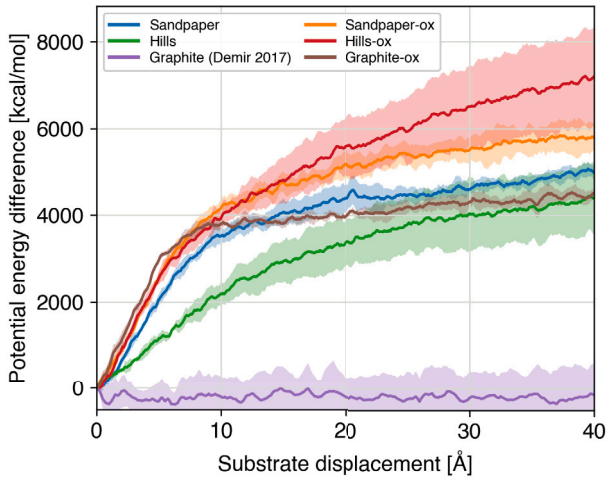

Fig. 5. Replica and pullout direction averaged potential energy difference curves as a function of substrate lateral displacement for the plain composite systems. Shaded regions indicate one standard deviation from the mean. Data for graphite taken from Ref. [50].

CF displacements in the hills composites that were aligned with the corrugation produced the lowest potential energy difference response.

For context, the purple line shows the potential energy difference of a *pristine* four-layer graphite epoxy composite of similar unit cell dimensions, using data from Ref. [50], and is essentially zero over all displacement distances. The potential energy difference response for the composite comprising an oxidized version of graphite exhibits unique behavior, with the largest energy difference of $3500\,\mathrm{kJ\,mol^{-1}}$ up to about 8 Å of displacement, which then plateaus for the remaining displacement distances up to an ultimate value of just over $4000\,\mathrm{kJ\,mol^{-1}}$ similar to the ultimate mean value for the plain hills composite. The characteristic response of the potential energy difference in both the sandpaper composites and the hills composites is similar between the plain and oxidized variants, albeit with an overall increase in potential energy difference for the oxidized cases. Furthermore, the large difference between aligned and anti-aligned CF displacement and corrugation direction in the hills CF was preserved after oxidation, indicating that surface oxidation does not interfere with the interfacial mechanism of the corrugation effect. This increased potential difference in the oxidized cases appears to be proportional with CF displacement distance, with the oxidized sandpaper composite resulting in the smallest overall increase relative to the plain case, and the oxidized hills composite yielding in the greatest.

A proxy measure for the ultimate interfacial shear strength of a composite is the ISS, which was calculated for all composites at a CF displacement of 40 Å. Fig. 6 presents these replica and displacement direction averaged ISS data, comparing the plain and oxidized values for each type of CF structure. ISS values of all oxidized composites were greater than their plain counterparts, with the graphite composite exhibiting the largest change from effectively zero for the plain case to 31(1) MPa. Interestingly, the addition of oxygen groups does not yield a uniform increase in the ISS for all CF surfaces, suggesting that there may be competing effects at play as a result of the oxidation process. The hills CF showed the second highest ISS increase after oxidation, with an ISS of 31(6) MPa and increasing to 50(8) MPa after oxidation. The sandpaper CF exhibited the lowest ISS increase with a plain composite value of 36(1) MPa which increased to 40(2) MPa after oxidation. Observing the trends in ISS, improvements via oxidation treatment are most effective when the CF has large domains of relatively flat surface. Presumably, oxidation on flat portions of the CF allows for greater engagement with the polymer matrix, perhaps by accommodating matrix packing that enables more interaction between electronegative sites of the matrix, and the CF oxidation. However, it is not possible to completely decouple the chemistry effect of the oxidation from the additional topography induced by the oxidation process. For the sandpaper CF, it may be that the roughness lengthscale, i.e. the distances between topographical peaks on the surface, is small enough such that the oxidation begins to effectively smooth out the surface presented to the polymer as the oxygen groups fill in surface undulations. Clearly, this smoothing effect was not strong enough to completely counter the additional chemical interactions between the polymer matrix and the surface functional groups.

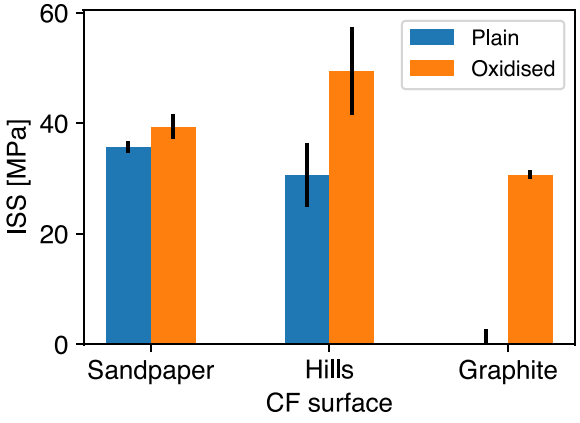

Fig. 6. Replica and displacement direction averaged ISS comparing the response of plain and oxidized composites, with error bars denoting one standard deviation from the mean. Data for plain graphite from Ref. [50].

To characterize the response of the polymer matrix under CF displacement, the displacement of the polymer itself was quantified after 40 Å of CF displacement. Displacement profiles of the polymer matrix were calculated by binning the total displacement of each polymer atom, in both longitudinal and transverse directions relative to the CF displacement direction, along the z coordinate perpendicular to the CF surfaces. Fig. 7 presents replica averaged polymer displacement distributions for both the longitudinal (solid lines) and transverse (dashed lines) displacements of atoms belonging to the polymer matrix are plotted as a function of the relative z coordinate of each composite, along the x (Fig. 7a) and y (Fig. 7b) directions.

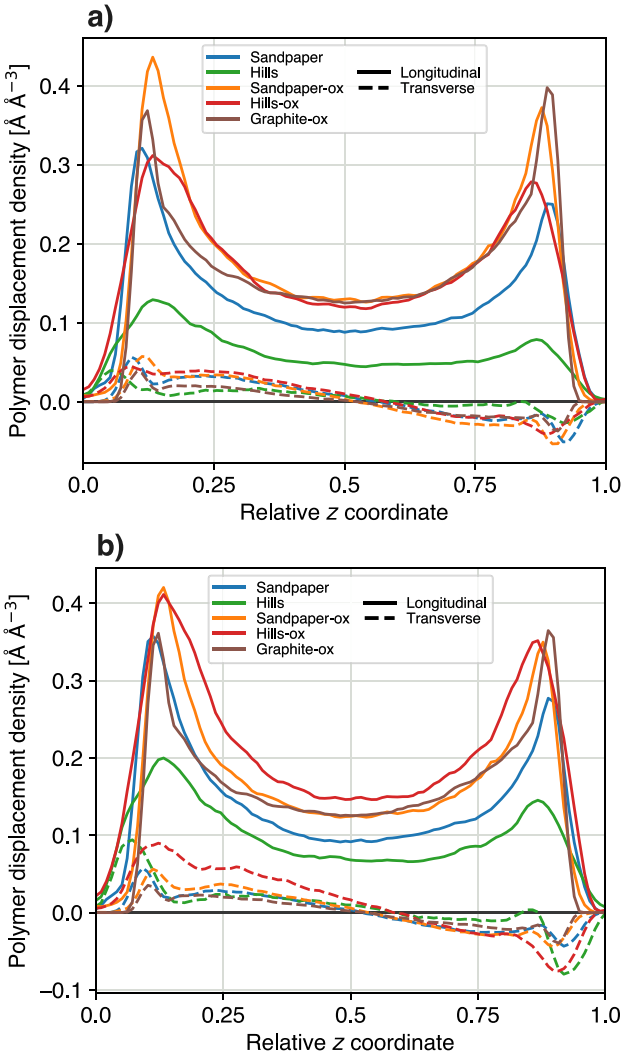

Fig. 7. Replica averaged polymer displacements as a function of simulation cell length z, perpendicular to the CF surface, for all composite systems. Displacements of polymer-only heavy atoms shown for displacements longitudinal and transverse to the CF displacement direction, shown with solid and dashed lines, respectively. Results for substrate displacement in the x and y direction is shown in panels (a) and (b), respectively.

The longitudinal displacement density may be also considered as a shear field of the matrix, with all composites exhibiting a similar behavior of high shear at the CF-matrix interfaces at approximately 0.12 and 0.88 relative z coordinate values, that tapers off to a minimum at the center of the matrix at a relative z of 0.5. It should be noted that due to slight variations in CF thickness between each model, the exact CF-matrix onset is located at slightly different relative z coordinates. A slightly different trend is present in the transverse displacement of the polymer which peaks at the CF-matrix interface and is followed by a trough before increasing and ultimately tapering off to zero at the center of the matrix. These slight troughs in the transverse polymer displacement indicate that standing compression waves that extend perpendicular from the CF surface may form during CF displacement, potentially due to the polymer structuring in the interphase region.

In the case of CF displacements in the x direction, the bulk matrix behavior is distinct between the oxidized and plain CF composites, with the hills composite exhibiting the lowest polymer shear, followed by the sandpaper composite. For CF displacement in y shown in Fig. 7b, once more the effect of corrugation-CF displacement alignment is apparent with an increase of not only the transverse component but also the shear longitudinal component of matrix displacement for both plain and oxidized hills composites. Comparing the polymer response for the hills composite with CF displacement aligned (Fig. 7a) and anti-aligned with the corrugation (Fig. 7b), the entire longitudinal profile is increased almost uniformly over the entire polymer region. This result indicates that the large scale corrugation not only increases the transfer of shear stress between CF and polymer at the interface, but is also effective in transferring the CF displacement throughout the interphase and into the polymer bulk. Note that a similar increase can be observed for the transverse polymer displacement profiles. For the best performing composite, the oxidized hills with anti-aligned CF displacement, the peaks of the longitudinal polymer displacement in the interphase were similar to both the oxidized sandpaper and oxidized graphite, however the bulk-like polymer displacements were greater than all other composites studied.

Hydrogen bonding analysis was performed on the three oxidized composite interfaces during CF displacement simulations by calculating the number of donating and accepting hydrogen bonds every picosecond during CF displacement. Intra-matrix hydrogen bond counts, shown in Figs. 8a and 8c, and CF-matrix hydrogen bond counts, shown in Figs. 8b and 8d, each exhibit similar curve characteristics for all oxidized interfaces. The number of inter-matrix hydrogen bonds initially increase for all interfaces, then plateau for displacements past 30 Å. The one exception to this trend is for oxidized hills CF surfaces under y CF displacements, which appear to continue to increase up to the ultimate displacement of 40 Å. Oxidized graphite surfaces plateau to a slightly lower hydrogen bond count relative to the rough oxidized surfaces which exhibit similar curves under x coordinate CF displacements. When combined with the polymer displacement data shown previously, these results make intuitive sense. Surfaces with global corrugation can apply a greater transverse stress to the polymer matrix when CF displacements are anti-aligned with the corrugation, thereby resulting in an increase in intra-matrix hydrogen bonding as the matrix is compressed.

CF-matrix hydrogen bond counts were found to be similar for hills and sandpaper oxidized surfaces under both x (Fig. 8b) and y (Fig. 8d) CF displacement, with an initial decrease followed by a plateau. oxidized graphite surfaces yield similar curves, with a slightly increased initial value, indicating greater hydrogen bonding between CF and matrix prior to CF displacement.

The polymer displacement and hydrogen bonding data suggests that there are two separate factors that may impact the mechanical response of the composite interface under CF displacement. First the initial traction between CF and matrix at the interface itself, which may be affected by both nanoscale roughness and chemical interactions via oxidation. Second, the ability of both the matrix *and* the CF to transfer the applied load to the interphase region of the matrix. This can be affected by ensuring that the polymer network topology is minimally compromised in the interphase, and by the presence of large global corrugations in the CF surface which could potentially apply compressive loads to the matrix during CF displacement thereby engaging the strongly connected bulk matrix region during CF displacement events.

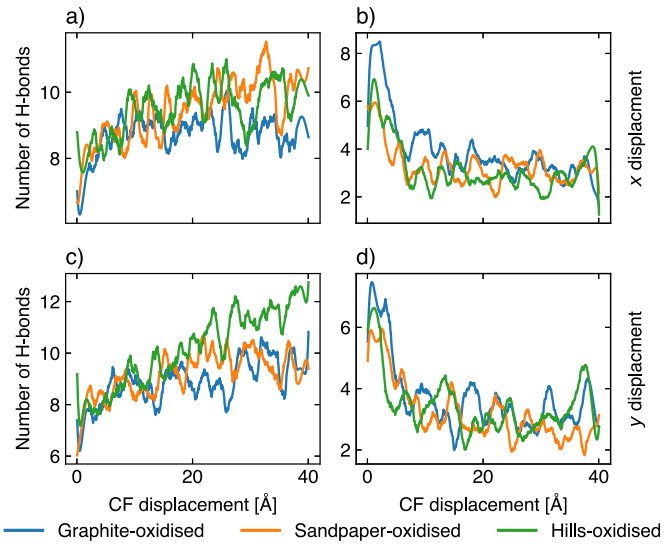

Fig. 8. Replica average number of intra-matrix (panels a and c), and CF-matrix (panels b and d) hydrogen bonds, shown for CF displacements along x and y unit cell directions.

4. Conclusions

Molecular dynamics simulations of novel topographically and chemically rich CFRC interfaces have been used to decouple the impact of two factors that affect the mechanical response of the CF-matrix interface: intrinsic nanoscale roughness of the CF surface; and chemical interaction due to oxygen functional groups on the surface. These simulations of rough non-oxidized interfaces provide a more appropriate benchmark of ISS for pristine CFRCs beyond that of a pristine graphite composite. After oxidation treatments, CF surfaces that had large graphitic (relatively flat) surface domains exhibited the greatest increase in ISS relative to their un-oxidized state. According to these data, an optimal heavily oxidized CF surface is one with nanoscale surface corrugation that can effectively transfer the shear load up beyond the matrix interphase and into the bulk-like matrix, with the length-scale between surface peaks such that high oxygen functional group loading does not fill in the surface topography presented to the matrix. To summarize, we find that both nanoscale surface roughness and chemical interaction from oxygen bearing groups can enhance the ISS, but that the addition of oxygen groups may also effectively smooth out the CF surface, thereby reducing the enhancement effect.

Further characterization of the matrix at the interphase region has also revealed a disconnected network topology exists in the interphase, suggesting that further improvement of interfacial interaction between CF and matrix could be achieved through targeted repair or crosslinking at the CF-matrix interface. In summary, these simulations provide unprecedented insights into the molecular-level details of the mechanical integrity of CFRC interfaces with realistic CF surfaces. Addressing these findings may inform novel targeted next generation oxidation procedures applied during CF production, and provides a roadmap towards further improving the interfacial shear stress of the fiber matrix interface under tensile loading conditions.

CRediT authorship contribution statement

Filip Vuković: Writing – review & editing, Writing – original draft, Visualization, Validation, Software, Methodology, Investigation, Formal analysis, Conceptualization. **Ben Newman:** Methodology, Investigation, Formal analysis. **Yanting Yin:** Methodology, Formal analysis. **Gunther G. Andersson:** Methodology, Formal analysis, Data curation, Conceptualization. **Luke C. Henderson:** Supervision, Resources, Investigation, Conceptualization. **Tiffany R. Walsh:** Writing – review & editing, Supervision, Resources, Project administration, Methodology, Investigation, Funding acquisition, Conceptualization.

Declaration of competing interest

The authors declare the following financial interests/personal relationships which may be considered as potential competing interests: Tiffany R. Walsh reports financial support was provided by Office of Naval Research Global. Tiffany R. Walsh reports financial support was provided by Australian Research Council. If there are other authors, they declare that they have no known competing financial interests or personal relationships that could have appeared to influence the work reported in this paper.

Acknowledgments

This research was in part supported by Australian Research Council (ARC) Discovery Project DP180100094, and by the Office of Naval Research Global (N62909-18-1-2024). The authors acknowledge the facilities, and the scientific and technical assistance of Microscopy Australia (ROR: 042mm0k03) and the Australian National Fabrication Facility (ANFF) (ROR: 04ypnrn45), enabled by NCRIS and the government of South Australia at Flinders Microscopy and Microanalysis (ROR: 04z91ja70), Flinders University (ROR: 01kpzv902). FV thanks the Austrian Science Fund (FWF) for funding through grant 10.55776/P36264. Computational resources and services provided under the NCMAS scheme by the National Computational Infrastructure (NCI), which is supported by the Australian Government, are gratefully acknowledged.

Appendix A. Supplementary data

Supplementary Information is provided in the attached document.

Supplementary material related to this article can be found online at https://doi.org/10.1016/j.compscitech.2025.111354.

Data availability

Data will be made available on request.

References

[1] A.J. Timmis, A. Hodzic, L. Koh, M. Bonner, C. Soutis, A.W. Schäfer, L. Dray, Environmental impact assessment of aviation emission reduction through the implementation of composite materials, Int. J. Life Cycle Assess. 20 (2) (2014) 233–243.

[2] L. Zhu, N. Li, P. Childs, Light-weighting in aerospace component and system design, Propuls. Power Res. 7 (2) (2018) 103–119.

[3] G.M. Lewis, C.A. Buchanan, K.D. Jhaveri, J.L. Sullivan, J.C. Kelly, S. Das, A.I. Taub, G.A. Keoleian, Green principles for vehicle lightweighting, Environ. Sci. Technol. 53 (8) (2019) 4063–4077.

[4] J. Fan, J. Njuguna, An introduction to lightweight composite materials and their use in transport structures, in: Lightweight Composite Structures in Transport, Elsevier, 2016, pp. 3–34.

[5] J.D.H. Hughes, The carbon fibre/epoxy interface—A review, Compos. Sci. Technol. 41 (1) (1991) 13–45.

[6] J.-K. Kim, Y. wing Mai, High strength, high fracture toughness fibre composites with interface control—A review, Compos. Sci. Technol. 41 (4) (1991) 333–378.

[7] D.J. Eyckens, F. Stojcevski, A. Hendlmeier, J.D. Randall, D.J. Hayne, M.K. Stanfield, B. Newman, F. Vuković, T.R. Walsh, L.C. Henderson, Carbon fibre surface chemistry and its role in fibre-to-matrix adhesion, J. Mater. Chem. A 9 (47) (2021) 26528–26572.

[8] H. Zheng, W. Zhang, B. Li, J. Zhu, C. Wang, G. Song, G. Wu, X. Yang, Y. Huang, L. Ma, Recent advances of interphases in carbon fiber-reinforced polymer composites: A review, Compos. B Eng. 233 (2022) 109639.

[9] M. Sharma, S. Gao, E. Mäder, H. Sharma, L.Y. Wei, J. Bijwe, Carbon fiber surfaces and composite interphases, Compos. Sci. Technol. 102 (2014) 35–50.

[10] P.W. Yip, S.S. Lin, Effect of surface oxygen on adhesion of carbon fiber reinforced composites, MRS Proc. 170 (1989).

[11] Y.Z. Wan, Y.L. Wang, Q.Y. Li, X.H. Dong, Influence of surface treatment of carbon fibers on interfacial adhesion strength and mechanical properties of PLA-based composites, J. Appl. Polym. Sci. 80 (3) (2001) 367–376.

[12] M.R. Alexander, F.R. Jones, Effect of electrolytic oxidation on the surface chemistry of type a carbon fibres-part i, X-ray photoelectron spectroscopy, Carbon 32 (5) (1994) 785–794.

[13] U. Zielke, K. Hüttinger, W. Hoffman, Surface-oxidized carbon fibers: I. Surface structure and chemistry, Carbon 34 (8) (1996) 983–998.

[14] D.J. Eyckens, F. Stojcevski, A. Hendlmeier, C.L. Arnold, J.D. Randall, M.D. Perus, L. Servinis, T.R. Gengenbach, B. Demir, T.R. Walsh, L.C. Henderson, An efficient high-throughput grafting procedure for enhancing carbon fiber-to-matrix interactions in composites, Chem. Eng. J. 353 (2018) 373–380.

[15] B. Demir, K.M. Beggs, B.L. Fox, L. Servinis, L.C. Henderson, T.R. Walsh, A predictive model of interfacial interactions between functionalised carbon fibre surfaces cross-linked with epoxy resin, Compos. Sci. Technol. 159 (2018) 127–134.

[16] Y. Yan, J. Xu, H. Zhu, Y. Xu, M. Wang, B. Wang, C. Yang, Molecular dynamics simulation of the interface properties of continuous carbon fiber/ polyimide composites, Appl. Surf. Sci. 563 (2021) 150370.

[17] S. He, T.R. Walsh, Prediction of chain-growth polymerisation of vinyl ester resin structure at the carbon fibre interface, Compos. Sci. Technol. 218 (2022) 109168.

[18] D.J. Eyckens, B. Demir, J.D. Randall, T.R. Gengenbach, L. Servinis, T.R. Walsh, L.C. Henderson, Using molecular entanglement as a strategy to enhance carbon fiber-epoxy composite interfaces, Compos. Sci. Technol. 196 (2020) 108225.

[19] E. Zussman, X. Chen, W. Ding, L. Calabri, D.A. Dikin, J.P. Quintana, R.S. Ruoff, Mechanical and structural characterization of electrospun PAN-derived carbon nanofibers, Carbon 43 (10) (2005) 2175–2185.

[20] C. Li, A.R. Browning, S. Christensen, A. Strachan, Atomistic simulations on multilayer graphene reinforced epoxy composites, Compos. A 43 (8) (2012) 1293–1300.

[21] Y. Hu, J.L. Ding, Effects of morphologies of carbon nanofillers on the interfacial and deformation behavior of polymer nanocomposites – A molecular dynamics study, Carbon 107 (2016) 510–524.

[22] X. Peng, S.A. Meguid, Molecular simulations of the influence of defects and functionalization on the shear strength of carbon nanotube-epoxy polymer interfaces, Comput. Mater. Sci. 126 (2017) 204–216.

[23] M. Zhang, X. Wang, M. Zhou, Z. Zhai, B. Jiang, The effect of self-resistance electric heating on the interfacial behavior of injection molded carbon fiber/polypropylene composites through molecular dynamics analysis, Polymer 207 (2020) 122915.

[24] T. Sohail, S. Nakarmi, R. Sweat, R. Baughman, H. Lu, S. Roy, Simulation of surface asperities on a carbon fiber using molecular dynamics and fourier series decomposition to predict interfacial shear strength in polymer matrix composites, Compos. Interface. 29 (8) (2022) 947–970.

[25] N. Subramanian, A. Rai, A. Chattopadhyay, Atomistically derived cohesive behavior of interphases in carbon fiber reinforced CNT nanocomposites, Carbon 117 (2017) 55–64.

[26] Z. Qin, K. Jin, M.J. Buehler, Molecular modeling and mechanics of acrylic adhesives on a graphene substrate with roughness, BioNanoScience 6 (3) (2016) 177–184.

[27] Y. Xin, F. Duan, X. Mu, Effects of defects on the interfacial shear characteristics between graphene and poly (methyl methacrylate), Polym. Compos. 41 (10) (2020) 4297–4306.

[28] S. Zhao, Y. Zhang, J. Yang, S. Kitipornchai, Improving interfacial shear strength between graphene sheets by strain-induced wrinkles, Carbon 168 (2020) 135–143.

[29] C. Zhang, H. Dai, Y. Lu, A model for calculation of carbon fiber composite interfacial performance based on molecular simulation and experiment, Compos. Comm. 53 (2025) 102235.

[30] Z. Li, W. Chen, D. Seveno, D. Jiang, Modeling and mechanism of the mechanical interlocking for the carbon fiber/epoxy interphase, Carbon 233 (2025) 119861.

[31] E. Fitzer, R. Weiss, Effect of surface treatment and sizing of C-fibres on the mechanical properties of CFR thermosetting and thermoplastic polymers, Carbon 25 (4) (1987) 455–467.

[32] G. Krekel, K.J. Hüttinger, W.P. Hoffman, D.S. Silver, The relevance of the surface structure and surface chemistry of carbon fibres in their adhesion to high-temperature thermoplastics, J. Mater. Sci. 29 (11) (1994) 2968–2980.

[33] J. Jiang, X. Yao, C. Xu, Y. Su, L. Zhou, C. Deng, Influence of electrochemical oxidation of carbon fiber on the mechanical properties of carbon fiber/graphene oxide/epoxy composites, Compos. A 95 (2017) 248–256.

[34] H. Fu, Y. Huang, L. Liu, Influence of fibre surface oxidation treatment on mechanical interfacial properties of carbon fibre/ polyarylacetylene composites, Mater. Sci. Technol. 20 (12) (2004) 1655–1660.
[35] X. Liu, C. Yang, Y. Lu, Contrastive study of anodic oxidation on carbon fibers and graphite fibers, Appl. Surf. Sci. 258 (10) (2012) 4268–4275.
[36] T. Semoto, Y. Tsuji, H. Tanaka, K. Yoshizawa, Role of edge oxygen atoms on the adhesive interaction between carbon fiber and epoxy resin, J. Phys. Chem. C 117 (47) (2013) 24830–24835.
[37] A. Shrestha, Y. Sumiya, K. Okazawa, T. Uwabe, K. Yoshizawa, Molecular understanding of adhesion of epoxy resin to graphene and graphene oxide surfaces in terms of orbital interactions, Langmuir 39 (15) (2023) 5514–5526.
[38] C. Jang, S. Nouranian, T.E. Lacy, S.R. Gwaltney, H. Toghiani, C.U. Pittman, Molecular dynamics simulations of oxidized vapor-grown carbon nanofiber surface interactions with vinyl ester resin monomers, Carbon 50 (3) (2012) 748–760.
[39] H. Wang, K. Jin, C. Wang, X. Guo, Z. Chen, J. Tao, Effect of fiber surface functionalization on shear behavior at carbon fiber/epoxy interface through molecular dynamics analysis, Compos. A 126 (2019) 105611.
[40] T. Li, Z. Meng, S. Keten, Interfacial mechanics and viscoelastic properties of patchy graphene oxide reinforced nanocomposites, Carbon 158 (2020) 303–313.
[41] F. Vuković, T. Walsh, Practical atomistic models of carbon fiber surfaces with tuneable topology and topography, Compos. Sci. Technol. 216 (2021) 109049.
[42] A.P. Thompson, H.M. Aktulga, R. Berger, D.S. Bolintineanu, W.M. Brown, P.S. Crozier, et al., LAMMPS - a flexible simulation tool for particle-based materials modeling at the atomic, meso, and continuum scales, Comp. Phys. Comm. 271 (2022) 108171.
[43] W.M. Brown, P. Wang, S.J. Plimpton, A.N. Tharrington, Implementing molecular dynamics on hybrid high performance computers - short range forces, Comp. Phys. Comm. 182 (2011) 898–911.
[44] W.M. Brown, A. Kohlmeyer, S.J. Plimpton, A.N. Tharrington, Implementing molecular dynamics on hybrid high performance computers - particle particle particle mesh, Comp. Phys. Comm. 183 (2012) 449–459.
[45] W.M. Brown, Y. Masako, Implementing molecular dynamics on hybrid high performance computers – three-body potentials, Comp. Phys. Comm. 184 (2013) 2785–2793.
[46] T.D. Nguyen, S.J. Plimpton, Accelerating dissipative particle dynamics simulations for soft matter systems, Comput. Mater. Sci. 100 (2015) 173–180.
[47] T.D. Nguyen, GPU-accelerated tersoff potentials for massively parallel molecular dynamics simulations, Comp. Phys. Comm. 212 (2017) 113–122.
[48] V. Nikolskiy, V. Stegailov, GPU acceleration of four-site water models in LAMMPS, in: Proceeding of the International Conference on Parallel Computing, ParCo 2019, Prague, Czech Republic, 2019.
[49] S.L. Mayo, B.D. Olafson, W.A. Goddard, DREIDING: a generic force field for molecular simulations, J. Phys. Chem. 94 (26) (1990) 8897–8909.
[50] B. Demir, L.C. Henderson, T.R. Walsh, Design rules for enhanced interfacial shear response in functionalized carbon fiber epoxy composites, ACS Appl. Mater. Inter. 9 (13) (2017) 11846–11857.
[51] N.A. Marks, Modelling diamond-like carbon with the environment-dependent interaction potential, J. Phys. Condens. Mat. 14 (11) (2002) 2901–2927.
[52] A.K. Rappé, W.A. Goddard, Charge equilibration for molecular dynamics simulations, J. Phys. Chem. 95 (8) (1991) 3358–3363.
[53] F. Vuković, Carbox, 2025, URL https://github.com/Fuzz-Muffin/CarbOx.
[54] A. Stukowski, Visualization and analysis of atomistic simulation data with OVITO–the open visualization tool, Modelling Simul. Mater. Sci. Eng. 18 (1) (2009) 015012.
[55] A. Stukowski, Computational analysis methods in atomistic modeling of crystals, JOM 66 (3) (2013) 399–407.
[56] H. Edelsbrunner, E.P. Mücke, Three-dimensional alpha shapes, ACM T. Graph. 13 (1) (1994) 43–72.
[57] C. Hontoria-Lucas, A.J. López-Peinado, J.D. López-González, M.L. Rojas-Cervantes, R.M. Martín-Aranda, Study of oxygen-containing groups in a series of graphite oxides: Physical and chemical characterization, Carbon 33 (11) (1995) 1585–1592.
[58] F. Hopfgarten, Surface study of carbon fibres with ESCA and auger electron spectroscopy, Fibre Sci. Technol. 11 (1) (1978) 67–79.
[59] Z. Yue, W. Jiang, L. Wang, S. Gardner, C. Pittman, Surface characterization of electrochemically oxidized carbon fibers, Carbon 37 (11) (1999) 1785–1796.
[60] A.J. Marsden, M. Skilbeck, M. Healey, H.R. Thomas, M. Walker, R.S. Edwards, N.A. Garcia, F. Vuković, H. Jabraoui, T.R. Walsh, J.P. Rourke, N.R. Wilson, From graphene to graphene oxide: the importance of extended topological defects, Phys. Chem. Chem. Phys. 24 (4) (2022) 2318–2331.
[61] L. Martínez, R. Andrade, E.G. Birgin, J.M. Martínez, PACKMOL: A package for building initial configurations for molecular dynamics simulations, J. Comput. Chem. 30 (13) (2009) 2157–2164.
[62] A.I. Jewett, D. Stelter, J. Lambert, S.M. Saladi, O.M. Roscioni, M. Ricci, L. Autin, M. Maritan, S.M. Bashusqeh, T. Keyes, R.T. Dame, J. Shea, G.J. Jensen, D.S. Goodsell, Moltemplate: A tool for coarse-grained modeling of complex biological matter and soft condensed matter physics, J. Mol. Biol. 433 (11) (2021) 166841.
[63] J.R. Gissinger, B.D. Jensen, K.E. Wise, REACTER: A heuristic method for reactive molecular dynamics, Macromolecules 53 (22) (2020) 9953–9961.
[64] J.R. Gissinger, B.D. Jensen, K.E. Wise, Modeling chemical reactions in classical molecular dynamics simulations, Polymer 128 (2017) 211–217.
[65] B. Demir, T.R. Walsh, A robust and reproducible procedure for cross-linking thermoset polymers using molecular simulation, Soft Matter 12 (8) (2016) 2453–2464.
[66] J.W. Martin, C. de Tomas, I. Suarez-Martinez, M. Kraft, N.A. Marks, Topology of disordered 3D graphene networks, Phys. Rev. Lett. 123 (11) (2019).